Journal of Non-Crystalline Solids 499 (2018) 300–308

Contents lists available at ScienceDirect

Journal of Non-Crystalline Solids

journal homepage: www.elsevier.com/locate/jnoncrysol

Raman scattering and molecular dynamics investigation of lead metasilicate glass and supercooled liquid structures

D.V. Sampaio[a,*], A. Picinin[a], Benjamin J.A. Moulton[a], J.P. Rino[a], P.S. Pizani[a], E.D. Zanotto[b]

[a] Universidade Federal de São Carlos, Departamento de Física, Caixa Postal 676, 13565-905 São Carlos, SP, Brazil
[b] Universidade Federal de São Carlos, Departamento de Engenharia de Materiais, Caixa Postal 676, 13565-905 São Carlos, SP, Brazil

ARTICLE INFO

Keywords:
Raman spectroscopy
Molecular dynamics
Glass structure
Lead metasilicate
Depolymerization

ABSTRACT

In this research we correlate the structural parameters obtained from molecular dynamics (MD) simulations and Raman scattering to construct a self-consistent picture of the glass structure, and its variation from ambient temperature to the supercooled liquid above the glass transition temperature (Tg). The MD results show that the glass structure is composed of SiO_4 tetrahedra and PbO_x (x = 4, 5) polyhedra. To correlate the Q^n population obtained from the MD and Raman a second type of Q^3 species is required. The two types of Q^3 species are interpreted as being associated with the bimodal distribution displayed by the Pb−Si pair correlation function. From a MD snapshot is also shown that the second Q^3 species can have a bridging oxygen bound to a Pb ion. As the temperature increases, depolymerization of the Q^n speciation is observed and confirmed by the oxygen speciation determined from both Raman and MD. The depolymerization of the silica network is consistent with the non-Arrhenian (fragile) viscosity decrease with temperature and may explain this viscosity behavior.

1. Introduction

Investigation of glass and supercooled liquid structures at high temperatures is of prime importance to understand glass properties, to tailor the composition of new functional glasses, and to describe natural phenomena, such as igneous processes [1, 2]. Silicate glass structures can be described in terms of building blocks having well-established short-range order, the silica tetrahedron (SiO_4) [2]. In pure silica glass, each SiO_4 is corner linked to four other SiO_4 (Q^4 units), forming a tridimensional "molecular" network where bridging-oxygen anions (BO) are bound to adjacent Si cations, −Si−O−Si−. The addition of modifier cations (M), such as Na or Pb, induces depolymerization of the silica network through the breakdown of −Si−O−Si− linkages, forming non-bridging oxygen anions (NBO), −Si−O−M. This depolymerization process creates tetrahedra that have different proportions of BOs and NBOs. These units are called Q^n species, where *n* represents the average number of BO per tetrahedron. Therefore, the Q^n species distribution yields insights into the connectivity of the silica network.

The $PbO{\cdot}SiO_2$ (PS) is an important model for the glass community and its isochemical crystal phase melts congruently [3]. Moreover, lead silicate glasses are of considerable scientific interest because they have an outstanding glass forming ability despite having equal or less than 50 mol% of SiO_2 [4], so-called inverted glasses. Several investigations have reported the Q^n species of lead silicate glasses (Table 1). For example, the MD simulations of Cormier et al. [5] calculated the dominant Q^n species as being Q^2, at 41%. Using nuclear magnetic resonance (NMR) experiments, Fayon et al. [6] found that Q^2 is 51% of the total Q^n, while Feller et al. [7] obtained 38% Q^2, and Schneider 47% (± 8%) [8]. More recently, Kacem et al. [9] obtained a population of 59% of Q^2 using Raman spectroscopy. Despite some numerical differences (Table 1), all these studies show that the PS glass at room temperature has a Q^n distribution centered on the Q^2 species, similar to its isochemical crystal.

In addition to the NBO and BO, some oxygen atoms may not be bound to Si atoms at all, the so-called free oxygens (O^{-2}) [10–12]. These particular oxygen atoms are referred here to as non-network oxygen (NNO); they are not bound to any Si atom but can be bound to M cations [13]. For example, an oxygen atom may be bound to two M cations via M-O-M linkages. For PS glass, Cormier et al. [5], using MD simulations, computed 36.6% of BOs, 60.0% of NBOs and 3.4% of NNOs. Based on the NMR experiments of Lee et al. [14], 36% of the total oxygen atoms are estimated to be BO, 62% are NBO and 2% are NNO, whereas Dalby et al. [15] obtained 42.6% of BOs from X-ray photoelectron spectroscopy experiments. Additionally, X-ray scattering, neutron scattering and computer simulations have also been used to study other structural parameters, e.g., first neighbor distances, coordination numbers and bond-angle distributions [4, 5, 16, 17]. Based on these parameters, it has been suggested that PS is composed by two

* Corresponding author.
E-mail addresses: davidvsampaio@gmail.com, dvsampaio@df.ufscar.br (D.V. Sampaio).

https://doi.org/10.1016/j.jnoncrysol.2018.07.048
Received 26 December 2017; Received in revised form 14 July 2018; Accepted 17 July 2018

Table 1
Q^n distributions (%) of PS glass from previous studies.

Reference	Method	Q^0	Q^1	Q^2	Q^3	Q^4
Cormier et al. [5]	MD	2	19	42	30	7
Fayon et al. [6]	NMR	0	13	51	30	6
Schneider et al. [8]	NMR	0	21	47	26	6
Feller et al. [7]	NMR	6	25	38	25	6
Kacem et al. [9]	Raman	2	24	59	12	3

*These variations are partially due to the use of different techniques and fitting procedures, and also due to the glass samples being made (quenched) at different cooling rates.

subnetworks, one formed by the SiO_4 and the other formed by PbO_x (x = 3 to 5) polyhedra [16, 17].

Despite the numerous studies on PS glass structure, there is a lack of knowledge about the structural modifications that take place at high temperatures above Tg. Recently, Rodrigues et al. [18] showed that a combination of Raman spectroscopy and molecular dynamics simulations (MD) are a particularly good method for investigating the variation of glass structure with temperature. The Raman technique accesses the vibrational modes of the material, which for glasses are often very similar to the vibrational density of states calculated by MD. On the other hand, MD make use of the Raman spectrum to calibrate the energy scale to describe the structural properties [18]. Moreover, Raman spectroscopy permits the determination of the Q^n distribution [9], while the MD, can also describe the atomic structure via calculation of the pair correlation functions and bond-angle distributions, in addition to the Q^n population [5, 17]. As a result, it is possible to describe an insightful picture of a given glass structure and its temperature dependence.

In the present research, we determine the structural evolution with temperature of the PS glass and supercooled liquid. We stress the connection between Raman spectroscopy and MD simulation as a powerful combination to investigate glass properties and the development of structural models.

2. Materials and methods

2.1. Molecular dynamics simulation

The effective interaction potential proposed to describe the PS system has the same functional form as those used to study other oxide systems, like $BaSi_2O_5$ and $Ba_{1-x}K_xBiO_3$ [18–20]. It consists of a steric repulsion due to size effects, Coulomb interactions due to charge transfer between ions, charge-induced dipole due to the electronic polarizability of ions, and the van der Waals attraction. The interatomic potential reads

$$V(r) = A\left(\frac{\sigma_i + \sigma_j}{r}\right)^{\eta_{ij}} + \frac{Z_i Z_j}{r}\exp\left(-\frac{r}{\lambda}\right) - \left(\frac{\alpha_i Z_j^2 + \alpha_j Z_i^2}{2r^4}\right)\exp\left(-\frac{r}{\xi}\right) - \frac{W_{ij}}{r^6}. \quad (1)$$

here, A is the strength of the steric repulsion, σ is the ionic radii of the ions i and j, η_{ij} the exponent of the repulsion term, Z the effective charge of ions, α the electronic polarizability, and W_{ij} the van der Waals intensity. λ and ξ are the screening lengths for Coulomb and charge-dipole interactions, respectively. A cutoff distance, r_c, was introduced and the potential was shifted, therefore the potential itself and its first derivative were null at the cutoff distance.

The parameters shown in Table 2 were fit to reproduce the correct energy and length scales at the experimental density and zero pressure. The length scale was verified by comparing the simulated static structure factor with reported results from neutron diffraction experiments, while Raman scattering provided the energy scale necessary to determine the effective charges.

We report here a system with 15,000 particles (3000 Pb + 3000 Si + 9000 O atoms). All simulations were done in a NPT ensemble

Table 2
Set of the two-body potential parameters used in the MD simulation.

	Pb	Si	O
Z (*e*)	0.81570	1.63140	−0.81570
σ (Å)	1.22	0.45	1.44
α (Å^3)	1.0	0.0	3.0

	Pb−Pb	Pb−Si	Pb−O	Si−Si	Si−O	O−O
A (eV)	0.63346	0.63346	0.63346	0.63346	0.63346	0.63346
W (eVÅ^6)	0	0	243.689	0	0	0
η	11	9	7	11	9	7

λ = 6.0 Å, ξ = 3.0 Å, r_c = 10.0 Å.

using the LAMMPS program assuming time steps of 1.0 fs. Starting from a very hot liquid, which was thermalized by 100,000 time steps, the system was cooled down at a rate of $6.66{\cdot}10^{12}$ K/s to the desired temperature where the properties were analyzed. At each temperature, the system was thermalized by 20,000 time steps, and the results were obtained from an additional 20,000 time steps.

The structural properties were analyzed for their two- and three-body correlations. The pair distribution function, coordination numbers, static structure factor, and bond-angle distribution are discussed below; please check [18] for the definition of these quantities. The vibrational density of states was obtained from a Fourier transformation of the velocity-velocity auto-correlation function, whereas the Q^n distribution as a function of temperature was calculated from the phase space trajectories. The estimated molecular dynamics glass transition temperature, Tg^{MD}, is around 950 K ± 50 K. This value was obtained by comparing the structural relaxation time (τ) at different temperatures and the experimental observation time, t_{obs}. The observation time was determined by $t_{obs} = (\mathrm{dlogt/dt})^{-1}$, and the relaxation time was determined through a non-exponential fit of the incoherent intermediate scattering function $F_s(q,t)$ [21, 22]. T_g^{MD} was defined as the temperature where $\tau \sim t_{obs}$.

2.2. Experimental procedure

A 100 g $PbO{\cdot}SiO_2$ glass sample was made by mixing ground quartz SiO_2 (Vitrovita, Brazil) and Pb_3O_4 (Sigma-Aldrich, USA) in the stoichiometric ratio. Afterwards, the mixture was melted in a platinum crucible for two hours and then quenched between two steel plates. The glass used in this study is that of batch 2 from Cassar et al. [3]. The Raman measurements were done using a Horiba-Jobin-Yvon HR800 Evolution micro-Raman spectrometer using a 532 nm wavelength laser as the excitation source and a 50× long work distance objective. All measurements were taken in-situ, using a 1 mm sized sample mounted in a Linkam TS1500 micro-furnace. The spectra were collected using the 1800 slits/mm grating between 600 and 1300 cm^{-1} with a laser power of 1 mW at the sample. Each spectrum is an average of five 60 s measurements. Before each measurement we waited 5 min for temperature stabilization, taking 10 min at each temperature step in total. Wavenumbers were calibrated against the position of the silicon peak (520.7 cm^{-1}), and the experimental results were normalized by the experimental T_g^{DSC} = 687 K.

For the Raman curve fitting, we used the Fityk (0.9.8) software [23]. The high-frequency bands are assumed to have Gaussian line-hapes. The first step was to fit the baseline using a cubic function, where only the intensities of the Gaussians were left free, the Levemberg-Marquardt fitting algorihm was used. Then, the band center positions, and later the full-width at half-maximum (FWHM) were permitted to vary freely, where the Nelder-Mead Simplex fitting algorihm was used to fit them. As a result, at the last step of the curve fitting, no constraints in the Gaussians or the baseline were imposed, and all parameters were let free. However, this procedure does not mean that

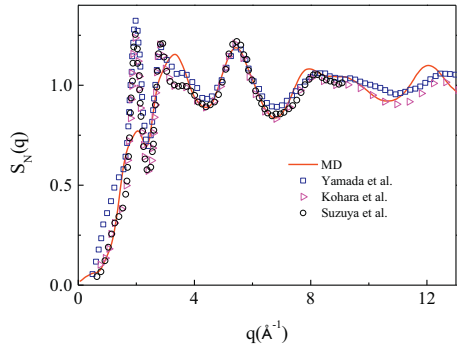

Fig. 1. - Structure factor calculated from the MD simulation (line) compared with neutron diffraction data [16, 24, 25]. The reasonable agreement, even in long range correlation, supports the reliability of the MD simulation.

no constraints in the curve fitting procedure were used. Details about these constraints to the curve fitting procedure are discussed in the next sections.

3. Results and discussion

3.1. Molecular dynamics simulation at room temperature

It is of major importance to show that the MD model reproduces the experimental results. The first test was to compare the calculated total neutron static-structure factor with experimental data. A good agreement in both shape and position of the neutron diffraction peaks between the calculated and experimental data was observed (Fig. 1) [16, 24, 25]. According to Kohara et al. [16], the position of the first sharp diffraction peak at 2 Å^{-1} indicates that the network is not formed only by linked SiO_4 units, corroborating the idea that some lead atoms can also act as a network former.

The second structural probe used to validate the MD model was Raman spectroscopy. The calculated vibrational density of states is compared with the Raman spectrum in Fig. 2. The MD vibrational density of states was obtained from Fourier transform of the velocity auto-correlation [18]. The simulation reproduces most vibrational modes of PS, especially in the high frequency region (800–1200 cm^{-1}) that is characteristic of the Q^n species.

The starting point to understand the glass structure from the MD simulation is to examine the atomic arrangement. This arrangement is described by the calculated pair correlation function $g_{ab}(r)$, the coordination number $C_{ab}(r)$ and the bond-angle distribution. Fig. 3 shows all $g_{ab}(r)$, which characterizes the distance distribution between a pair

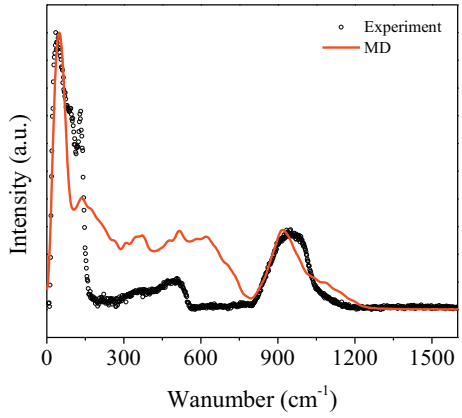

Fig. 2. Comparison between the Raman spectrum (background removed) and the MD calculated vibrational density of states. The MD model reproduces most features of the Raman spectrum.

of ions, and $C_{ab}(r)$ that characterizes their respective coordination number for a given radius. The analysis of the first neighbor distances were carried out by fitting a lognormal function(s). When necessary, a Gaussian function was added in order to simulate the tail of the second neighbor. Table 3 shows the obtained values using the lognormal functions and the curve fits are presented in the supplementary material (S. 1). The coordination numbers were obtained from the calculation of the $C_{ab}(r)$ based on the $g_{ab}(r)$ curve fit for a given cutoff distance by integrating the individual contribution of each lognormal.

The $g_{Si-O}(r)$ has only one contribution centered at 1.65 Å, which is characteristic of the Si—O distance in tetrahedra-based silicate compounds [26]. The coordination number C_{Si-O} is four, as expected of a tetrahedral geometry. The bond-angle distributions of O—Si—O and O—O—O are centered at 109° and 60°, respectively, confirming the tetrahedral geometry (Fig. 4). Additionally, the bond-angle distribution of Si—O—Si, which represents the connectivity between two SiO_4 units, shows a broad band between 120° and 180° (Fig. 4). This broad distribution is characteristic of (disordered) corner-sharing tetrahedra in silicate glasses. Moreover, the Si—Si pair distribution shows two distinct distances, one centered at 3.11 Å and another at 3.25 Å, with $C_{\underline{Si}\text{-}Si}$ values of 1.11 and 0.96, respectively and corroborates the corner-sharing SiO_4 network.

The $g_{Pb-O}(r)$ shows two contributions, one intense peak centered at 2.30 Å and a small peak at 2.59 Å. The individual coordination numbers are 4.27 and 1.08, respectively. This bimodal distribution was also seen in X-ray and neutron scattering experiments [4, 16], and by MD simulations [17]. The peak positions presented here agree with these literature results, but there are small discrepancies in the individual coordination numbers. The discrepancies are attributed to the fact that the first and second coordination shells are not well defined. Consequently, the values of C_{Pb-O} reported in the literature vary from 4.0 to 5.8 [5, 16, 17, 27]. The O—Pb—O angle distribution has two peaks (Fig. 4), at 60° and 90°, with a wide distribution to higher angles, which is in agreement with published data [16, 17, 27]. This angular distribution correlates with the radial distribution results indicating that the Pb is present in distorted PbO_4 polyhedral, with some PbO_5 also present. This interpretation concurs with the results of Rybicki et al. [17] and Kohara et al. [16], who suggested that the majority of Pb is found in PbO_4 units for the PS composition. A representative snapshot to show the Pb environment was made using the Ovito software [28] and it is shown in Fig. 5. It can be observed that Pb_1 and Pb_2 are coordinated by four oxygen atoms, sharing an edge, and each oxygen atom is bound to at least one Si atom.

3.2. Q^n speciation at room temperature

The Q^n speciation can be obtained from the curve fit of the high-frequency Raman spectrum, where each species is found in a specific frequency range [9, 29–31]. In the present case, two different curve fit models were used (Fig. 6) and the fit parameters are in Table 4. The first (M1) was proposed by Kacem et al. [9], based on the investigation of a series of binary lead silicates. Their model assume that the high-frequency Raman band of PS can be decomposed into six Gaussians corresponding to Q^0 (844 cm^{-1}), Q^1 (890 cm^{-1}), Q^2 (960 cm^{-1}), Q^3 (1004 cm^{-1}), T_{2s} (1057 cm^{-1}), and Q^{4II} (1131 cm^{-1}) [9]. However, the assignment of the 1050 cm^{-1} band as a T_2 vibration is controversial (see next paragraph for details). Instead, some authors have assigned the 1050 cm^{-1} band as a Q^3 vibration [30–32]. This controversy leads us to our model M2, where the 1050 cm^{-1} vibration is considered as an additional Q^3 species ($Q^{3'}$). Moreover, some constraints are considered during the curve fitting procedure of M2:

- Use the same number of Gaussians proposed by Kacem et al. [9]
- The Gaussian band parameters should be in the range observed by Kacem et al. [9].
- Each Gaussian should not be completely enveloped by another band.

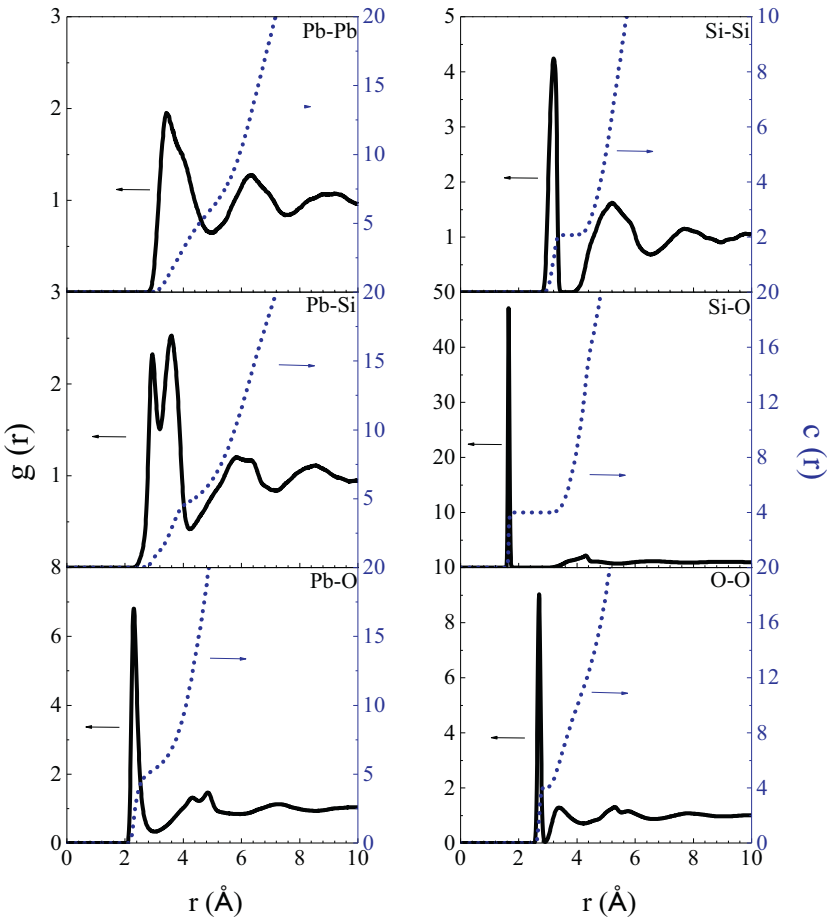

Fig. 3. All partial correlation functions and their respective coordination for PS glass. Note that the pair correlation functions related to Pb do not achieve null values, which makes the coordination not well defined. The bimodal distribution is easily seen for Pb—Si, that is further correlated with the second type of Q^3 species (details in the text).

Table 3
First neighbor distances, full-width at half-maximum (FWHM) and coordination numbers (CN) for each pair of ions, calculated from lognormal decomposed g(r) functions. Cells with two values reflect the bimodal distribution for the given pair. The last two columns present the values from Ref. [16].

Atomic pair	First neighbor dist. (Å)	FWHM (Å)	CN	First neighbor dist. (Å) [16]	CN [16]
Pb—Pb	3.48, 4.20	0.81, 0.63	3.59 + 1.98	–	–
Si—Si	3.11, 3.25	0.26, 0.19	1.11 + 0.96	–	–
Pb—Si	2.94, 3.58	0.34, 0.72	0.77 + 3.46	–	–
Si—O	1.65	0.08	4.00	1.63	4.0
Pb—O	2.30, 2.59	0.26, 0.44	4.27 + 1.08	2.32, 2.77	2.8 + 1.3
O—O	2.70	0.14	4.00	2.65	4.2

- The Q^n population should agree with that obtained by other methods.

Le Losq et al. [33] have attributed the 1050 cm^{-1} band to a T_2 vibrational mode of the TO_4 tetrahedra, where two oxygens move closer to the central Si while the other two oxygens move away. Consequently, this contribution is not included in the Q^n calculation of M1. In contrast, McMillan et al. [30] have suggested that this band could be assigned to symmetric stretching vibrations for a range of Q^3 groups in a distribution of structural environments; a second type of Q^3. This second type of Q^3 was first suggested by Matson et al. [32], studying alkali-silicate glasses, where they attributed the frequency shift from the normal Q^3 to the "crowd" effect, regions with a higher concentration of alkali modifiers. Recently, a similar suggestion was made by O'Shaughnessy et al. [31], when studying different compositions of

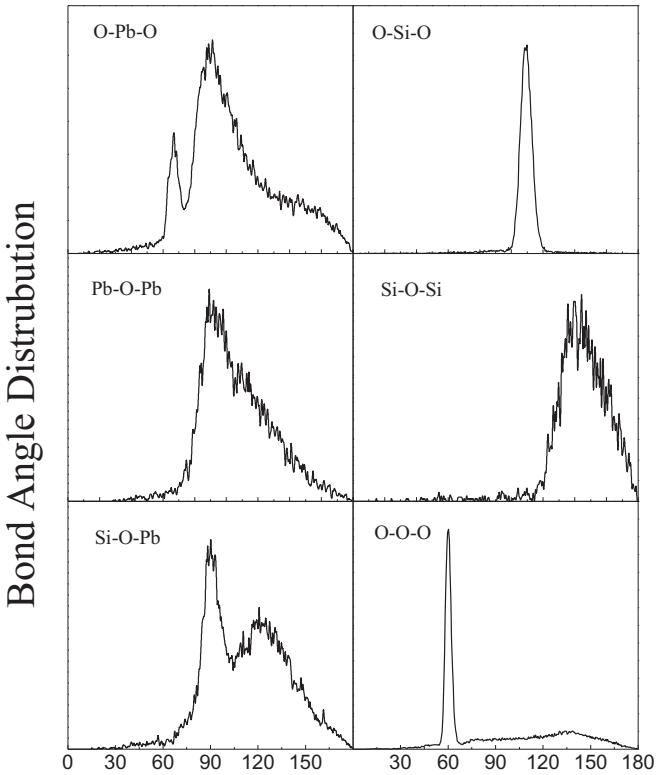

Fig. 4. Selected bond-angle distributions characterizing the tetrahedral geometry of the SiO_4 and the Pb polyhedra.

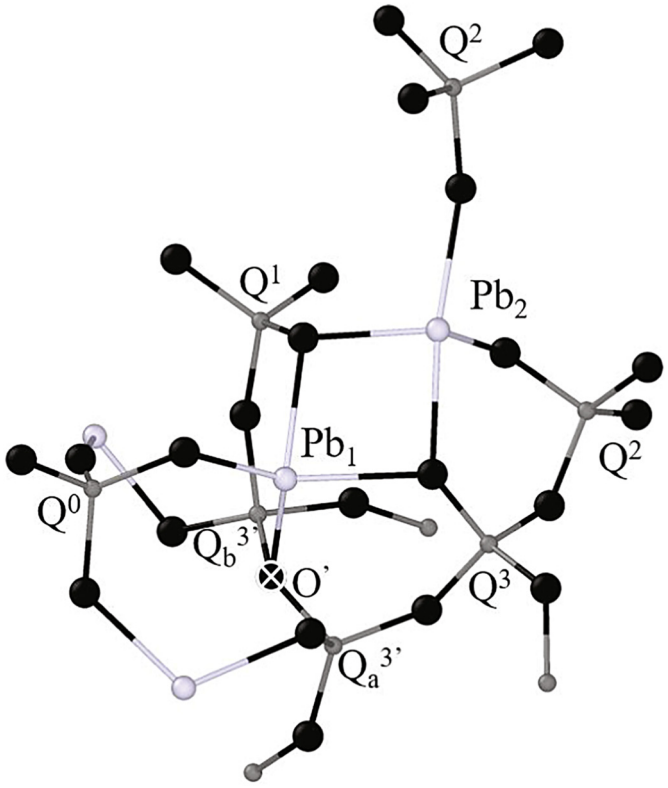

Fig. 5. Representative snapshot from MD simulation of the PS glass. Pb atoms are in silver, oxygen in black and Si in medium grey. Above, each Pb atom is coordinated by four oxygens where two of the oxygens form an edge sharing geometry. Each oxygen bound to the Pb atoms is also bound to a Si atom, composing different Q^n species. The snapshot also shows two different types of Q^3. A common Q^3 (r_{Si-Pb} = 3.45 Å) and the second Q^3 type, $Q^{3'}$ (r_{Si-Pb} = 2.92 Å for $Q_a^{3'}$ and 3.12 Å for $Q_b^{3'}$). Moreover, note that the $Q^{3'}$ have one BO (O′, crossed oxygen) that is also bonded to the Pb_1 ion.

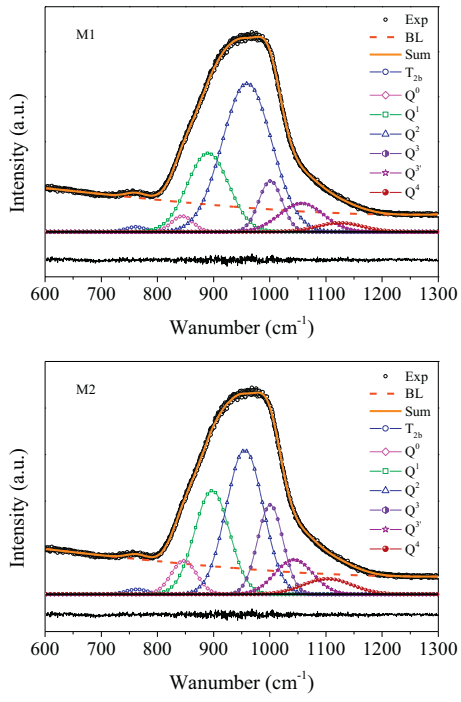

Fig. 6. Curve fits of the high-frequency region at room temperature. Both models, M1 and M2, reproduce the experimental data.

Table 4
Fit parameters of M1 and M2 models.

M1	Freq. (cm^{-1})	FWHM (cm^{-1})	Area (Norm.)
Q^0	844	45	0.02
Q^1	890	86	0.23
Q^2	959	104	0.53
Q^3	1001	49	0.09
T_{2s}	1056	92	0.09
Q^4	1124	94	0.03
M2	**Freq. (cm^{-1})**	**FWHM (cm^{-1})**	**Area (Norm.)**
Q^0	847	54	0.07
Q^1	897	73	0.25
Q^2	955	78	0.38
Q^3	1001	53	0.16
$Q^{3'}$	1043	79	0.09
Q_4	1103	103	0.05

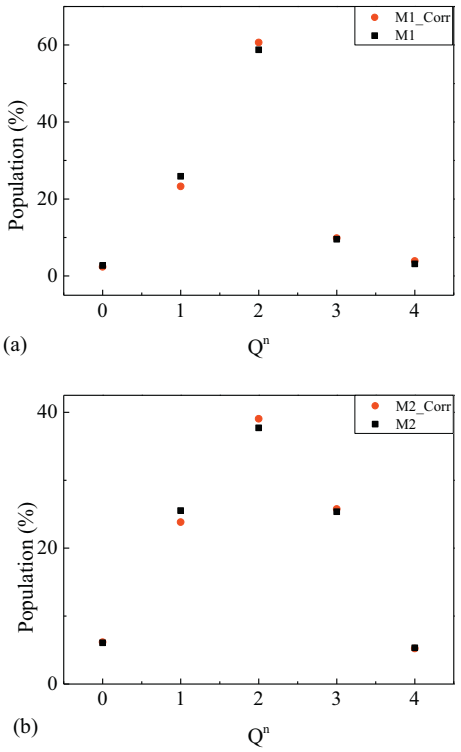

Fig. 7. Q^n population of M1 and M2 obtained from the corrected spectrum (circles) and uncorrected with cubic baseline (squares). The corrected and uncorrected give the same results in both models, indicating that such a correction is not necessary for this glass.

$(x)Cs_2O-(100-x)SiO_2$ glasses. O'Shaughnessy et al. [31] assumed that each Q^n species has a second type, related to two distinct populations of BO, one bound only to two Si atoms, and another bound to two Si and a modifier. Consequently, the 1050 cm^{-1} band is considered to be an additional Q^3 species when calculating the Q^n population. Therefore, our second model (M2) interprets the 1050 cm^{-1} band to be another type of Q^3, labeled as $Q^{3'}$ (Fig. 6).

To extract the Q^n species from a Raman spectrum, it is common for authors to apply the Long correction for frequency and temperature effects (Eq. 2) [29, 30]. However, the literature is not clear about this correction for high frequencies [34].

$$I = I_{obs}\cdot\left\{\nu_0^3\cdot\nu\frac{[1-\exp(-hc\nu/kT)]}{(\nu_0-\nu)^4}\right\} \quad (2)$$

here, h is the Planck constant, c is the speed of light, k is the Boltzmann

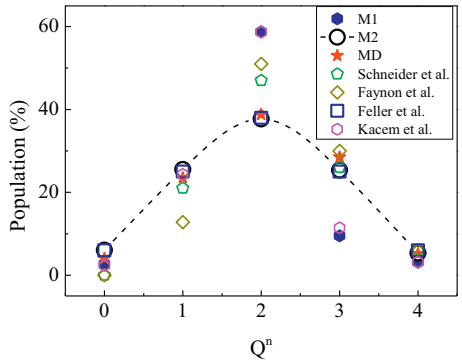

Fig. 8. Comparison of Q^n species at room temperature of this work and literature data [6–9]. The M1 reproduces the results of Kacem et al. [9]. However, M2 shows a better agreement with NMR [7] and our MD results.

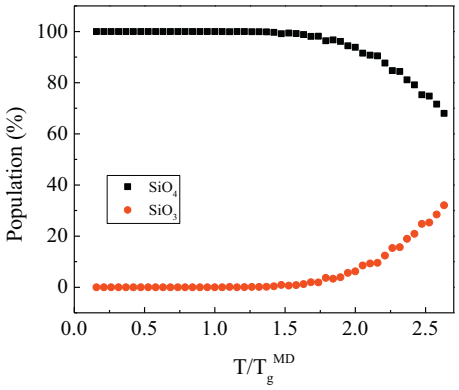

Fig. 10. Proportion of fourfold, tetrahedral Si and threefold Si with temperature. Note the decrease in the number of SiO_4 is balanced by the appearance of SiO_3 units after 1.5 T_g^{MD}. All temperatures used are in Kelvin.

constant, T is the absolute temperature, ν_0 is the wavenumber of the incident laser light, and ν is the measured wavenumber in cm^{-1}. To evaluate the real need for this correction for our PS glass spectra, each model is fit with and without the correction. Both corrected and uncorrected approaches yield the same results for the M1 and M2 models (Fig. 7). Therefore, we conclude that the use of the temperature-frequency correction for the Q^n speciation is unnecessary for these spectra.

Several experimental data are available for the Q^n population at room temperature for the PS glass (Table 1). However, it is worth

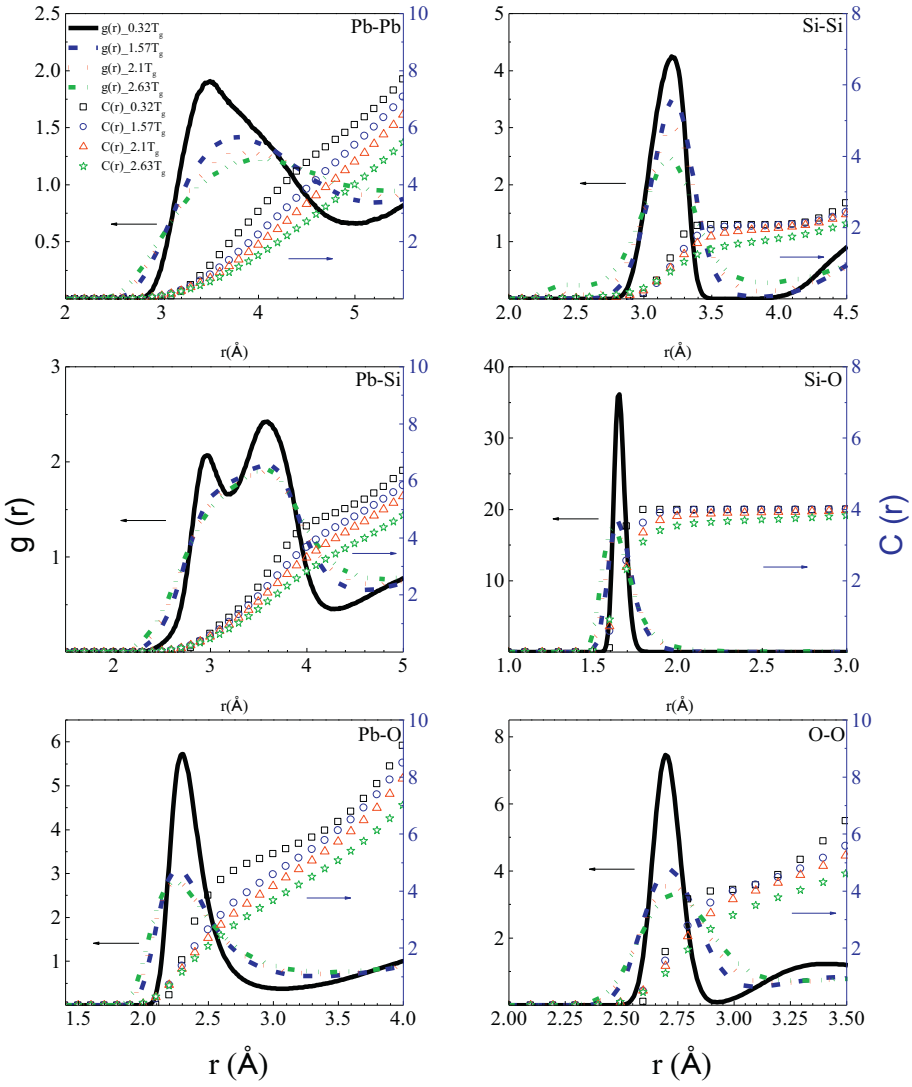

Fig. 9. Temperature dependence of g(r) and C(r) showing the general broadening of all g(r) with increasing temperature. Note the decrease in the Si—O coordination number which is associated with the appearance of SiO_3 units (See Fig. 10).

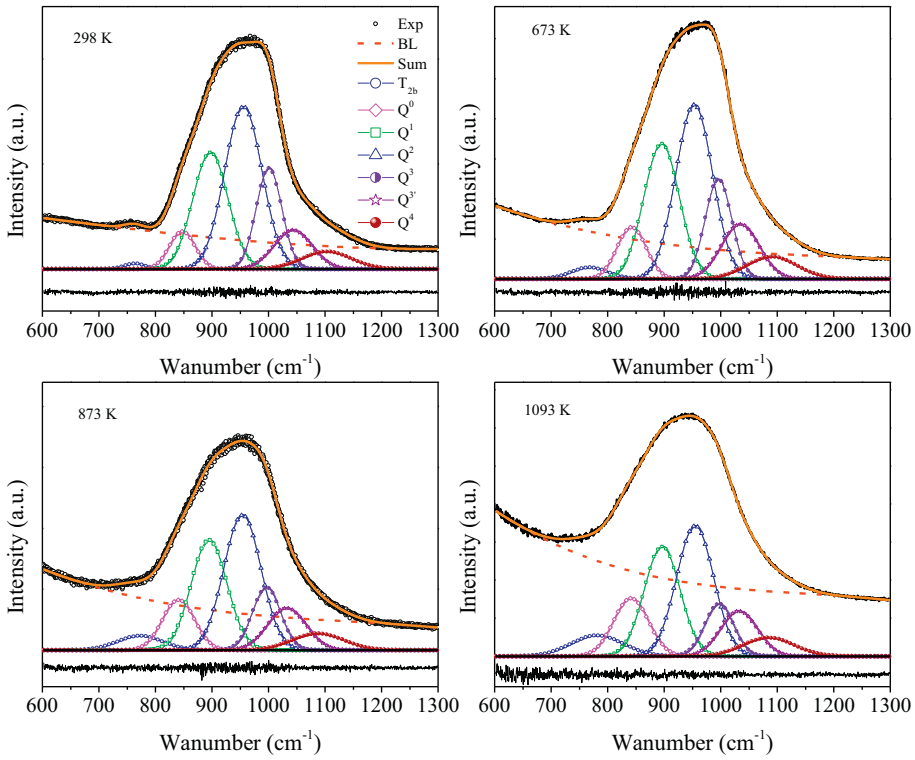

Fig. 11. Selected in-situ high temperature Raman spectra and their respective curve fit using M2 model. Legends are used throughout all curves. Other temperatures are in supplementary material.

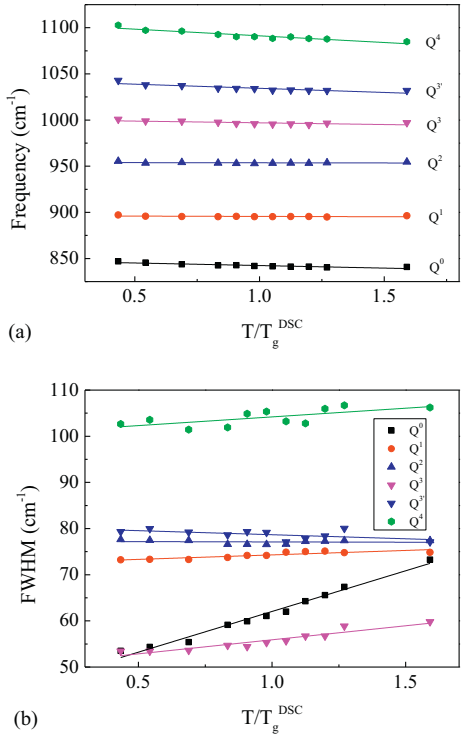

Fig. 12. Variation of the frequency (a) and FWHM (b) with temperature. The frequency shift displays a small decrease for all Q^n species whereas the FWHM show different behaviors depending on the Q^n species. Temperatures are in Kelvin.

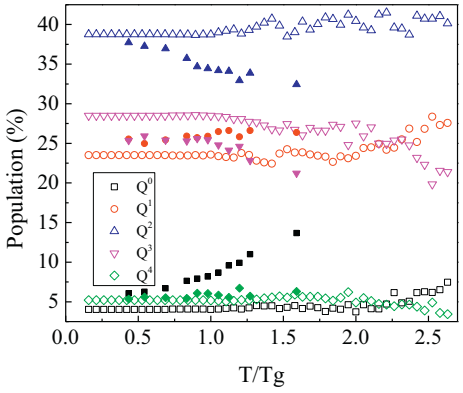

Fig. 13. Q^n population as a function of temperature determined from the M2 model (full dots) and MD simulations (empty symbols). The general behavior of Q^n shows a depolymerization of the glass with temperature. Temperatures are in Kelvin, normalized by T_g^{DSC} and T_g^{MD} for Raman and MD results, respectively.

mentioning that Kacem et al. [9] is the only source of Raman data, while all others were derived from NMR measurements [6–8]. The Q^n distributions from M1, M2, and MD results are compared with the literature in Fig. 8 [6–9]. Note that M1 model reproduces the results obtained by Kacem et al. [9], even though the Long correction was not used by us. However, the Q^3 population determined using the M1 model significantly diverges when compared with all NMR literature and also with our MD result. This discrepancy suggests that the M1 model, and therefore the interpretation of the 1050 cm^{-1} band as a T_{2s} vibration is not adequate to explain the Q^n distribution. In contrast, the Q^n population of our M2 model yields a very good agreement with that of the MD and NMR results. In fact, the M2 model reproduces the MD and NMR [7] Q^n distributions within 3% or better. Therefore, the interpretation of the 1050 cm^{-1} band as a $Q^{3'}$ species yields a more realistic Q^n distribution.

The interpretation of a second Q^3 type has been used by many authors based on different techniques [30–32, 35–39]. From our MD

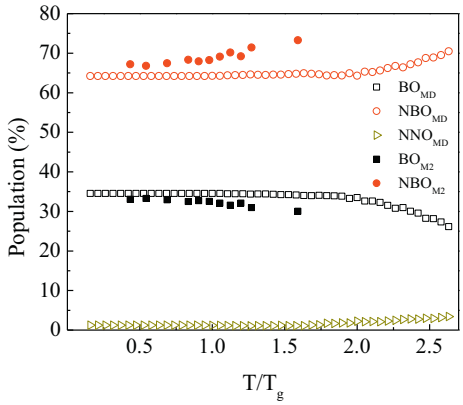

Fig. 14. Proportions of BOs, NBOs and NNOs calculated using: Raman Q^n species (full dots); MD simulation (empty dots). Both methods show the same qualitative behavior of depolymerization as the temperature increases. Temperatures are in Kelvin, normalized by T_g^{DSC} and T_g^{MD} for Raman and MD results, respectively.

Table 5
Oxygen speciation at room temperature comparing this work with literature results [5, 14].

	This Work Raman (%)	This Work MD (%)	Cormier et al. [5] (%)	Lee et al. [14] (%)
BO	33	34.6	36.6	36
NBO	67	64.2	60	62
NNO	0	1.2	3.4	2

simulations, we suggest that the two distinct Q^3 species in PS glass are related to the bimodal distribution shown in the pair correlation function $g_{Pb-Si}(r)$ (Fig. 3). The closest Si—Pb distance represents a stronger interaction between the SiO_4 unit and the Pb cation. This is reflected in the Raman spectrum as a shift to higher frequencies and leads to $Q^{3'}$ signal around 1050 cm^{-1}. Whereas the distant Si—Pb correlation, the common Q^3, shows a Raman signal around 1000 cm^{-1}. These two types of Q^3 are shown in the MD snapshot (Fig. 5). The common Q^3 with a Si—Pb distance of 3.44 Å, and the $Q^{3'}$ which has a Si—Pb distance of 2.98 Å. Note that one of the BOs (O′) in the $Q^{3'}$ is also bound to the Pb_1 ion (Fig. 5). The existence of the O′ species endorses the speculation of O'Shaughnessy et al. [31] regarding to an additional Q^3 species and it is justified herein by the observation in the MD snapshot.

3.3. Temperature effects

The g(r) and C(r) are analyzed to describe the structural behavior with temperature (Fig. 9). Independent of the pair of ions, g(r) becomes broader with increasing temperature and, consequently, the first and second coordination shells become less defined. However, it can be noted that C_{Si-O} shows a decrease in the coordination number after $1.5T_g^{MD}$. This phenomenon is reflected in the number of SiO_4 units as a function of temperature, where some Si become threefold coordinated, SiO_3 units, above $1.5T_g^{MD}$ (Fig. 10).

The Q^n species are also investigated as a function of temperature. In order to compare the MD Q^n speciation with the Raman results, we only considered in the MD the Si atoms composing a SiO_4. The Raman curve fitting procedure as a function of temperature required additional constraints:

- The curve fit of the previous temperature was used as the starting point for the next higher temperature.
- No abrupt change in the curve parameters is expected from one temperature to the next. This includes the frequency and FWHM of each Gaussian band.
- We maintained a constant number of Gaussians for the entire temperature range.

Both M1 and M2 models reproduce the high temperature Raman data and show similar qualitative Q^n behaviors (see Supplementary material S.2 and S.3). However, quantitatively, the discrepancies between the M1 and MD are even greater at high temperature. Therefore, only the M2 and MD results are reported in the high temperature curve fits (Fig. 11), the Q^n distribution (Fig. 13) and the oxygen speciation (Fig. 14).

All curve fit reproduces the experimental Raman spectra from room temperature to 1093 K (Fig. 11). The peak center frequency of all Gaussian curves shows a small linear decrease as temperature increases due to anharmonic effects (Fig. 12a). FWHMs also show a linear behavior as temperature increases, where the strongest variation is observed in the Q^0 species (Fig. 12b). The Q^n speciation, obtained from the Raman curve fits and MD (Fig. 13), show similar behaviors as a function of temperature. In both, Raman and MD, the Q^3 abundance decreases while Q^1 and Q^0 increase without significant changes in the proportion of Q^4. The major discrepancy is that the Q^2 species decreases in the M2 model while it slightly increases in the MD simulation. Despite this discrepancy, these results show a depolymerization of the silicate network resulting from an increase in the overall number of NBO with increasing temperature (Fig. 14).

In order to elucidate the depolymerization process, the oxygen speciation was computed (Fig. 14). First, from the Raman Q^n speciation using the total oxygen given by the stoichiometry, and second, computed directly from the MD simulations accounting for all 9000 oxygen atoms in the system. Details about the calculations are provided in the supplementary material (S. 4). The MD calculations yield 64.2%, 34.6% and 1.2% for the proportion of BO_{MD}, NBO_{MD} and NNO_{MD}, respectively. On the other hand, the Raman analysis shows that 33% are BO and 67% are NBOs without any NNOs required. These values are in good agreement with previous MD study of Cormier et al. [5] and recent NMR experiments from Lee et al. [14] (Table 5). The temperature dependence of these species shows a consumption of BO to produce NBOs (Fig. 14). Additionally, the NNO_{MD} show only a small variation with temperature, from 1.2% to 2.6%. These results confirm a depolymerization in the lead metasilicate glass as the temperature increases and may explain the non-Arrhenious viscosity decrease reported in the literature, e.g. Cassar [3].

4. Conclusions

The combination of Raman spectroscopy and molecular dynamics simulations provided a detailed description of the PS glass structure and its temperature dependence throughout he SCL sate. We suggest that PS glass and supercooled liquid have two distinct Q^3 species and that these two Q^3 species are related to the bimodal distribution of the Pb—Si pair correlation function. Additionally, we also show that the $Q^{3'}$ species can also have BOs bound to Pb ions. In fact, to correctly calculate the Q^n distribution from the Raman spectra it is necessary to include both Q^3 species. With increasing temperature, there is a decrease in the Q^3 species to the benefit of Q^0 and Q^1 species indicating the (expected) depolymerization of the network. Our results show that this depolymerization occurs from the consumption of BOs to form NBOs and minor amounts of NNOs, which may explain the stunningly non-Arrhenian viscosity decrease with temperature.

Acknowledgements

We are grateful to Ricardo F. Lancelotti, Dr. Alisson M. Rodrigues and Dr. Daniel R. Cassar of LaMaV- DEMa- UFSCar for providing the PS glass samples. We also thank the São Paulo Research Foundation (FAPESP) for funding this research through CEPID grant #2013/07793-6 and post-doctoral grants # 2016/15962-0 and 2016/18567-5. Last

but not least, we would like to thank the two anonymous reviewers for their constructive comments and discussions.

Appendix A. Supplementary data

Supplementary data to this article can be found online at https://doi.org/10.1016/j.jnoncrysol.2018.07.048.

References

[1] J.C. Mauro, E.D. Zanotto, Two centuries of glass research: historical trends, current status, and grand challenges for the future, Int. J. Appl. Glas. Sci. 5 (2014) 313–327.
[2] G.S. Henderson, The structure of silicate melts: a glass perspective, Can. Mineral. 43 (2005) 1921–1958.
[3] D.R. Cassar, R.F. Lancelotti, R. Nuernberg, M.L.F. Nascimento, A.M. Rodrigues, L.T. Diz, E.D. Zanotto, Elemental and cooperative diffusion in a liquid, supercooled liquid and glass resolved, J. Chem. Phys. 147 (2017) 014501.
[4] T. Takaishi, M. Takahashi, J. Jin, T. Uchino, T. Yoko, Structural study on $PbO-SiO_2$ glasses by X-ray and neutron diffraction and 29Si MAS NMR measurements, J. Am. Ceram. Soc. 88 (2005) 1591–1596.
[5] G. Cormier, T. Peres, J.A. Capobianco, Molecular dynamics simulation of the structure of undoped and Yb^{3+}-doped lead silicate glass, J. Non-Cryst. Solids 195 (1996) 125–137.
[6] F. Fayon, C. Bessada, D. Massiot, I. Farnan, J.P. Coutures, 29 Si and 207 Pb NMR study of local order in lead silicate glasses, J. Non-Cryst. Solids 232 (1998) 403–408.
[7] S. Feller, G. Lodden, A. Riley, T. Edwards, J. Croskrey, A. Schue, D. Liss, D. Stentz, S. Blair, M. Kelley, A multispectroscopic structural study of lead silicate glasses over an extended range of compositions, J. Non-Cryst. Solids 356 (2010) 304–313.
[8] J. Schneider, V. Mastelaro, E. Zanotto, B.A. Shakhmatkin, N.M. Vedishcheva, A.C. Wright, H. Panepucci, Q^n distribution in stoichiometric silicate glasses: thermodynamic calculations and 29Si high resolution NMR measurements, J. Non-Cryst. Solids 325 (2003) 164–178.
[9] I. Ben Kacem, L. Gautron, D. Coillot, D.R. Neuville, Structure and properties of lead silicate glasses and melts, Chem. Geol. 461 (2017) 104–114.
[10] N. Nasikas, A. Chrissanthopoulos, N. Bouropoulos, S. Sen, G. Papatheodorou, Silicate glasses at the ionic limit: alkaline-earth sub-orthosilicates, Chem. Mater. 23 (2011) 3692–3697.
[11] H.W. Nesbitt, G.M. Bancroft, G.S. Henderson, R. Ho, K.N. Dalby, Y. Huang, Z. Yan, Bridging, non-bridging and free (O^{2-}) oxygen in Na_2O-SiO_2 glasses: an X-ray photoelectron spectroscopic (XPS) and Nuclear Magnetic Resonance (NMR) study, J. Non-Cryst. Solids 357 (2011) 170–180.
[12] J.F. Stebbins, Glass structure, melt structure, and dynamics: some concepts for petrology, Am. Mineral. 101 (2016) 753–768.
[13] G. Mountjoy, B.M. Al-Hasni, C. Storey, Structural organisation in oxide glasses from molecular dynamics modelling, J. Non-Cryst. Solids 357 (2011) 2522–2529.
[14] S.K. Lee, E.J. Kim, Probing metal-bridging oxygen and configurational disorder in amorphous lead silicates: insights from 17O solid-state nuclear magnetic resonance, J. Phys. Chem. C 119 (2014) 748–756.
[15] K.N. Dalby, H.W. Nesbitt, V.P. Zakaznova-Herzog, P.L. King, Resolution of bridging oxygen signals from O 1s spectra of silicate glasses using XPS: implications for O and Si speciation, Geochim. Cosmochim. Acta 71 (2007) 4297–4313.
[16] S. Kohara, H. Ohno, M. Takata, T. Usuki, H. Morita, K. Suzuya, J. Akola, L. Pusztai, Lead silicate glasses: binary network-former glasses with large amounts of free volume, Phys. Rev. B 82 (2010) 134209.
[17] J. Rybicki, A. Rybicka, A. Witkowska, G. Bergmański, A. Di Cicco, M. Minicucci, G. Mancini, The structure of lead-silicate glasses: molecular dynamics and EXAFS studies, J. Phys.: Condens. Matter 13 (2001) 9781.
[18] A.M. Rodrigues, J.P. Rino, P.S. Pizani, E.D. Zanotto, Structural and dynamic properties of vitreous and crystalline barium disilicate: molecular dynamics simulation and Raman scattering experiments, J. Phys. D Appl. Phys. 49 (2016) 435301.
[19] W. Jin, M.H. Degani, R.K. Kalia, P. Vashishta, Superconductivity in $Ba_{1-x}K_xBiO_3$, Phys. Rev. B 45 (1992) 5535.
[20] C.K. Loong, P. Vashishta, R.K. Kalia, W. Jin, M.H. Degani, D.G. Hinks, D.L. Price, J.D. Jorgensen, B. Dabrowski, A.W. Mitchell, Phonon density of states and oxygen-isotope effect in $Ba_{1-x}K_xBiO_3$, Phys. Rev. B 45 (1992) 8052.
[21] W. Kob, Computer simulations of supercooled liquids and glasses, J. Phys. Condens. Matter 11 (1999) R85.
[22] A. Cavagna, Supercooled liquids for pedestrians, Phys. Rep. 476 (2009) 51–124.
[23] M. Wojdyr, Fityk: a general-purpose peak fitting program, J. Appl. Crystallogr. 43 (2010) 1126.
[24] K. Yamada, A. Matsumoto, N. Niimura, T. Fukunaga, N. Hayashi, N. Watanabe, Short range structural analysis of lead silicate glasses by pulsed neutron total scattering, J. Phys. Soc. Jpn. 55 (1986) 831–837.
[25] K. Suzuya, D.L. Price, M.-L. Saboungi, H. Ohno, et al., Nucl. Instrum. Methods Phys. Res., Sect. B 133 (1997) 57–61.
[26] F. Liebau, Structural Chemistry of Silicates, (1985).
[27] T. Peres, D.A. Litton, J.A. Capobianco, S.H. Garofalini, Three-body potential modeling of undoped and Er^{3+}-doped lead silicate glass, J. Non-Cryst. Solids 221 (1997) 34–46.
[28] A. Stukowski, Visualization and analysis of atomistic simulation data with OVITO–the Open Visualization Tool, Model. Simul. Mater. Sci. Eng. 18 (2009) 015012.
[29] B.O. Mysen, L.W. Finger, D. Virgo, F.A. Seifert, Curve-fitting of Raman spectra of silicate glasses, Am. Mineral. 67 (1982) 686–695.
[30] P.F. McMillan, G.H. Wolf, B.T. Poe, Vibrational spectroscopy of silicate liquids and glasses, Chem. Geol. 96 (1992) 351–366.
[31] C. O'Shaughnessy, G.S. Henderson, H.W. Nesbitt, G.M. Bancroft, D.R. Neuville, Structure-property relations of caesium silicate glasses from room temperature to 1400K: implications from density and Raman spectroscopy, Chem. Geol. 461 (2016) 82–95.
[32] D.W. Matson, S.K. Sharma, J.A. Philpotts, The structure of high-silica alkali-silicate glasses. A Raman spectroscopic investigation, J. Non-Cryst. Solids 58 (1983) 323–352.
[33] C. Le Losq, D.R. Neuville, Effect of the Na/K mixing on the structure and the rheology of tectosilicate silica-rich melts, Chem. Geol. 346 (2013) 57–71.
[34] D.R. Neuville, D. de Ligny, G.S. Henderson, Advances in Raman spectroscopy applied to earth and material sciences, Rev. Mineral. Geochem. 78 (2014) 509–541.
[35] H. Maekawa, T. Maekawa, K. Kawamura, T. Yokokawa, The structural groups of alkali silicate glasses determined from 29Si MAS-NMR, J. Non-Cryst. Solids 127 (1991) 53–64.
[36] A.G. Kalampounias, S.N. Yannopoulos, G.N. Papatheodorou, A high-temperature Raman spectroscopic investigation of the potassium tetrasilicate in glassy, supercooled, and liquid states, J. Chem. Phys. 125 (2006) 164502.
[37] N. Trcera, S. Rossano, M. Tarrida, Structural study of Mg-bearing sodosilicate glasses by Raman spectroscopy, J. Raman Spectrosc. 42 (2011) 765–772.
[38] O.N. Koroleva, V.N. Anfilogov, A. Shatskiy, K.D. Litasov, Structure of Na_2O-SiO_2 melt as a function of composition: in situ Raman spectroscopic study, J. Non-Cryst. Solids 375 (2013) 62–68.
[39] S. Sen, R. Youngman, NMR study of Q-speciation and connectivity in K_2O-SiO_2 glasses with high silica content, J. Non-Cryst. Solids 331 (2003) 100–107.